

Ultrawideband reflection-mode optoacoustic mesoscopy

Murad Omar,^{1,2} Dominik Soliman,^{1,2} Jérôme Gateau,³ and Vasilis Ntziachristos^{1,2,*}

¹Chair for Biological Imaging, Technische Universität München, Ismaningerstr. 22, 81675, Munich, Germany

²Institute for Biological and Medical Imaging, Helmholtz Zentrum München, Ingolstaedter Landstr. 1, 85764, Neuherberg, Germany

³ESPCI ParisTech, PSL Research University, CNRS, INSERM, Institut Langevin, 1 rue Jussieu, F-75005, Paris, France

*Corresponding author: v.ntziachristos@tum.de

Received April 10, 2014; accepted May 17, 2014;

posted May 28, 2014 (Doc. ID 209917); published June 25, 2014

We developed a reflection-mode optoacoustic mesoscopy system, based on raster-scanning of a custom designed spherically focused ultrasound detector, enabling seamless epi-illumination of the volume imaged. We study the performance of acoustic-resolution mesoscopy operating at an ultrawideband bandwidth of 20–180 MHz, i.e., a frequency band spreading over virtually an order of magnitude. Using tomographic reconstruction we showcase previously unreported, to our knowledge, axial resolutions of 4 μm and transverse resolutions of 18 μm reaching depths of up to 5 mm. We further investigate the frequency-dependence of features seen on the images to understand the implications of ultrawideband measurements. We show the overall imaging performance and the frequency ranges that contribute to observable resolution improvements from phantoms and animals. © 2014 Optical Society of America

OCIS codes: (170.3010) Image reconstruction techniques; (170.3880) Medical and biological imaging; (170.3890) Optical optics instrumentation; (170.5120) Photoacoustic imaging; (110.5125) Photoacoustics.

<http://dx.doi.org/10.1364/OL.39.003911>

Morphogenesis refers to the process of organizing cells in ways so as to give certain shapes in organs and animals. It is a dynamic process that happens at multiple scales, from fast subcellular changes, to slow changes on the whole organ or organism level. Genetic alterations play a role in the shape and function of organisms [1], and imaging such changes is essential in experimental genetics. Optical microscopy techniques such as selective plane illumination microscopy are capable of imaging morphogenesis with high spatiotemporal resolution at the cellular and subcellular level, or the early stages of morphogenesis, such as in zebrafish larvae, or drosophila melanogaster embryos [1–3]. But because of light diffusion in larger biological organisms, or at depths greater than 500 μm in tissue, it becomes challenging to visualize morphogenesis at later stages of development [4].

We have recently considered raster-scan optoacoustic mesoscopy (R-SOM) to study fluorescent markers in drosophila pupae [5], an organism widely used in developmental biology, operating in transmission-mode. Using detection in the 25–125 MHz frequency range and reconstruction in tomographic mode, we showcased three-dimensional images with 30 μm in-plane (transverse), and 7 μm axial resolutions as deep as 5 mm in tissue. In contrast to optical-resolution optoacoustic microscopy [6–9], the in-plane resolution in optoacoustic mesoscopy is not defined by optical focusing capabilities but relies on the weakly scattering properties of ultrasound waves in tissue to provide ultrasonic diffraction-limited resolution, depending on the characteristics of the ultrasonic detection employed. This enables mesoscopy to reach deeper than optical microscopy or optical-resolution optoacoustic microscopy [4]. Compared to microscopy, the mesoscopic depth performance is better suited for imaging morphogenesis and function at later stages of development, where specimen size tends to be larger in diameter than one millimeter to a few millimeters.

Other systems operating in the mesoscopic regime worked with detectors that have a center frequency

ranging from 20 to 50 MHz; examples include, among others, a 24 MHz linear array [10], an all-optical scanner with frequencies as high as 39 MHz [11], and acoustic resolution optoacoustic microscopy systems operating with a single element spherically focused detector [12]. Our previous R-SOM implementation at 25–125 MHz was implemented in trans-illumination mode because the access for illuminating the sample around the focal zone of the detector and beyond was limited by the size of the detector, as shown in Fig. 1(a). This method was shown suitable for imaging thin samples only, where efficient light penetration can be achieved [5]. To improve the implementation of the method and gain access to larger samples, such as tumors, adult zebrafish, and to image samples that are prepared in special holders, where access is available only from one side, such as cell cultures, it was required that R-SOM operate in reflection mode. In

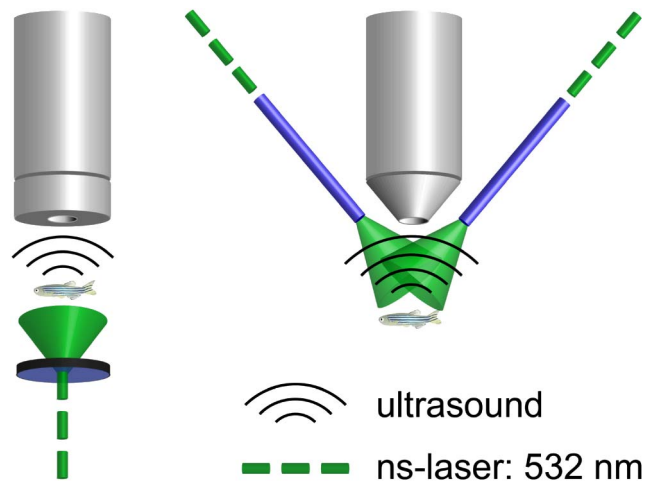


Fig. 1. (a) Sketch of the previous R-SOM implementation, (b) design of the new detector, with a customized conically shaped lens to allow for light to be coupled to the sample at an angle of 45°. [In (a) the violet disk is a diffusor; in (b) the violet rods are arms of a fiber bundle.]

addition, to improve the scalability of R-SOM, higher resolution was preferred than previous implementations.

Here, we present an arrangement that enables R-SOM imaging in reflection-mode, while improving the resolution of the technique. In particular, we custom designed and implemented an ultrasonic detector with a cone-shaped acoustic lens as shown on Fig. 1(b). This new design facilitates coupling of light from the same side, at an angle of 45° to the specimen. The spherically focused detector had an active element diameter of 1.5 mm, with an f-number ~ 1 , and operated at a center frequency of 98 MHz, with a previously unreported 20–180 MHz bandwidth, necessary for higher resolution imaging. The detector was connected through a low noise amplifier (63 dB, AU-1291, Miteq Inc., Hauppauge, New York, USA) to a high-speed digitizer, operating at 1 GS/s (CS122G1, Gage, Lockport, Illinois, USA; 12 bit resolution; max sampling rate, 2 GS/s). Illumination was provided by a 532 nm laser, with a pulse repetition rate of 2 kHz, energies of 1 mJ/pulse, and pulse widths of 0.9 ns (Wedge HB532, BrightSolutions SRL, Pavia, Italy). To perform fast acquisitions, the detector was scanned using fast piezo stages, in an alternating continuous-discrete manner. An area of 5 mm \times 5 mm was scanned at 10 μ m steps within approximately 2 min.

Image reconstruction was done using 3D beamforming with a dynamic aperture [5], to maintain a constant transverse resolution with depth. Compared to 2D beamforming [13], 3D beamforming achieved improved signal-to-noise ratio (SNR), reduced out of plane artifacts, and yielded isotropic in-plane resolution. The beamforming algorithm ran on a graphical processing unit, which accelerated the reconstruction by 2–3 orders of magnitude over CPU processing.

The system was characterized in terms of the resolution, and the depth of field achieved using 2 phantoms. Phantom 1 characterized the resolution achieved and consisted of 3 μ m spheres (polybead black dyed microspheres, Polysciences Inc., Warrington, Pennsylvania, USA). The microspheres were embedded in diffusive agar to mimic the optical scattering properties of tissue and are used to determine the point spread function of the system when using short laser pulses narrower than 1 ns [5,14]. Figure 2(a) shows a maximum intensity projection (MIP) of a 50 μ m slice at a depth of 100 μ m away from the detector focus and reveals isotropic in-plane resolution. The full width at half-maximum (FWHM) of the profiles from a single microsphere equals 18 μ m, and the FWHM of an axial profile from the same microsphere is 4 μ m, as shown in Fig. 2(b).

The penetration depth and possible resolution variation as a function of depth was characterized using a second phantom. Phantom 2 consisted of a knot made of a 10 μ m black suture embedded in optically diffusive agar. Depths of 2, 3, 4, and 5 mm were imaged by moving the knot away from the detector. Images were generated using 3D beamforming. Figure 2(c) shows the MIP of the suture at a depth of 5 mm. Figure 2(d) depicts the profiles recorded along the dotted line on Fig. 2(c), for the knot placed at different depths. The distance recorded between the two maxima of the reconstructed threads was found to be 30 μ m at a depth of 2 mm and it increases to 35 μ m at a depth of 5 mm.

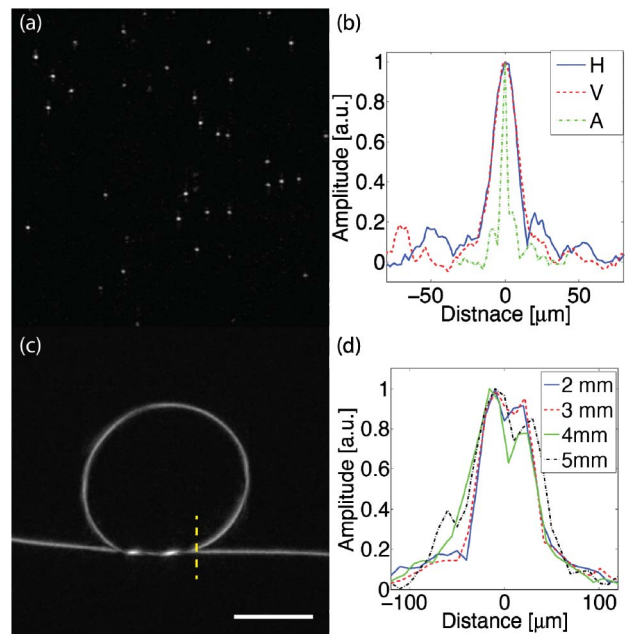


Fig. 2. (a) MIP of 3 μ m spheres at depths of 75–125 μ m away from the focus, (b) horizontal (H), vertical (V), and axial (A) profiles through one of the microspheres in (a), (c) MIP of a 10 μ m suture bent into a knot at a depth of 5 mm, (d) cross-section through the knot at different depths along the yellow line. Scale bar: (c) 1 mm.

To study the overall R-SOM performance and more specifically the effect of different frequency bands on the image, we first imaged a 1 week-old zebrafish (ZF) *ex vivo*, measuring 4 mm in length and 0.5 mm in diameter. The fish was embedded in low-melting agar. Figure 3(a) shows the MIP of the reconstruction of the ZF using the full bandwidth of the detector, 20–180 MHz. To reject noise outside the detection bandwidth the raw signals were band-pass filtered using an exponential filter of the 4th order. On the reconstruction several features of the ZF are seen, such as the lateral line (LL), the eyes (E), the melanocytes (M), and the intestines and heart of the fish (IH). Figure 3(b) shows a zoom-in image on the front part of Fig. 3(a). Figure 3(c) shows a MIP of the reconstruction of the ZF using the lower half of the detection bandwidth, i.e., 20–100 MHz. Figure 3(d) shows a MIP of the reconstruction using the upper half of the detection bandwidth, i.e., 100–180 MHz. Figure 3(d) is processed so that all pixels that have a lower value than the mean value of all the pixels are not shown (they were set to zero) to improve the visibility. Finally, Fig. 3(e) shows an overlay of Fig. 3(d) rendered in white, on Fig. 3(b) rendered in red. The arrows labeled (1) and (2) point to the same features across all the images.

The images reveal that the information in the upper band of the bandwidth recorded (>100 MHz) contributes to the image and is responsible for the high-resolution features observed. The amplitude of these high frequencies is inherently weaker than that of lower frequencies; they undergo higher attenuation and are recorded with lower SNR compared to larger features [15]. Because of this, when all the collected bandwidth is reconstructed in one inversion step, the low frequencies dominate

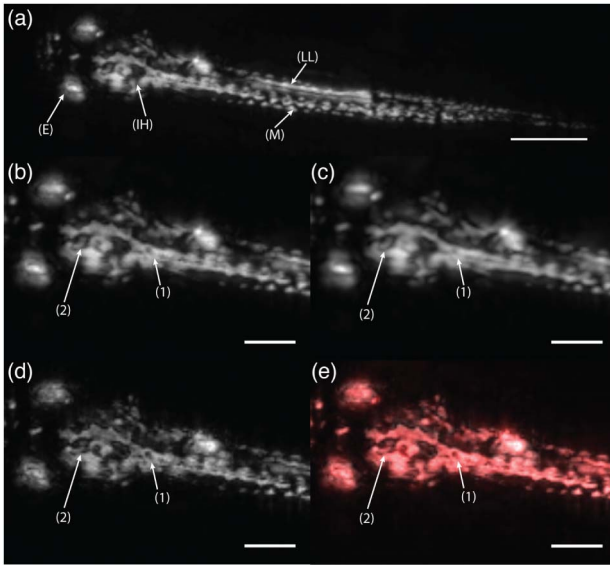


Fig. 3. (a) MIP of a zebrafish (ZF), (E) eye, (IH) intestines and heart, (M) melanocytes, (LL) lateral line, (b) zoom-in, showing the full bandwidth, (c) zoom-in on the low frequencies, 20–100 MHz, (d) zoom-in on the high frequencies, 100–180 MHz, (e) zoom-in on the overlaid image, red total image, and white high frequency image. Scale bars: (a) 500 μm , (b–e) 250 μm .

the image, and small features corresponding to high frequencies are not clearly visible on the images. This effect is observed by comparing Figs. 3(b)–3(d). However, separating the reconstruction to narrow frequency bands enables better handling of the noise, specific to each band, and better differentiation of the high frequency components. Figure 3(d) clearly reveals the high-resolution features in the image, which are not clearly visible on Fig. 3(b). For instance, arrow (1) points to a feature that looks almost as one piece in Figs. 3(b) and 3(c), while it becomes sharper, and more detailed in Fig. 3(d). Reconstructions from narrower bands also allowed better rendering of the information, by allowing, for example, the high frequency components to be plotted in a different color on the images.

To further investigate the capabilities of R-SOM we also imaged an excised mouse ear, which presents a microvasculature pattern at different scales. The mouse ear was fixed on a microscope slide with a transparent foil and imaged using the R-SOM. Figure 4(a) shows the MIP of the reconstruction of the full bandwidth of the detector, 20–180 MHz, Fig. 4(b) shows the MIP of the reconstruction of the low frequencies, 20–100 MHz, and Fig. 4(c) shows the MIP of the reconstruction of the high frequencies, 100–180 MHz. As in Fig. 3(d), a threshold was applied to Fig. 4(c), setting to zero all pixels with values lower than the mean intensity of all the pixels in the image, and another limit was set such that 0.4% of the pixels are saturated. Finally, Fig. 4(d) shows an overlay of Fig. 4(c) rendered in white, on Fig. 4(a) rendered in red. Applying multi-frequency reconstruction to the data collected from the mouse ear revealed vessels (Fig. 4(c)) that were otherwise invisible on the full-bandwidth image (Fig. 4(a)). Without separate processing of the high frequencies, Fig. 4(a) is dominated by low frequencies. The effect of the multi-frequency reconstruction is even more apparent in the case of

the mouse ear, as compared to the ZF. In the ZF the two-band frequency reconstruction improved the visibility of a few features that were otherwise smeared. But in the case of the ear, vessels that were invisible on Fig. 4(a) are seen on Fig. 4(c).

Broadband implementation of R-SOM was showcased herein and revealed a potent mesoscopy visualization modality. We interrogated the merits of the broadband response, which extended over almost an order of magnitude in the implementation herein. It was shown that reconstructions using data over narrow frequency bands might have advantages in broadband optoacoustic systems. This method is effective because different features can be reconstructed, processed, and rendered with frequency tailored tools, causing better performance in each frequency band. This improved performance was demonstrated herein simply by rendering the different frequencies in different colors and observing the improvements over the full bandwidth reconstructed image. Features corresponding to higher frequencies can be dominated by lower frequency components, which typically have higher intensity since sound attenuation increases with frequency. Treating the high frequencies separately also reduces the reconstruction noise, since only high-frequency noise is allowed in the image due to the filtering operation. Imaging performance could be further improved by separating the available bandwidth into even smaller bands, an area of current investigation.

Overall, R-SOM demonstrated high-resolution optoacoustic images of biological samples in the mesoscopy regime. The system achieved a resolution of 18 μm in-plane, and 4 μm axially, whereas the total penetration depth reached up to 5 mm, with virtually no degradation in resolution.

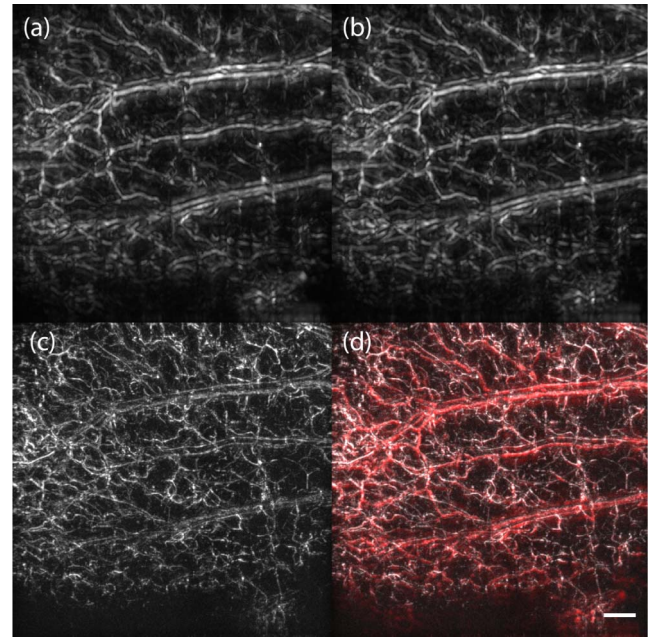


Fig. 4. (a) MIP of a mouse ear, the reconstruction was done using the full frequency range 20–180 MHz, (b) MIP of the mouse ear in the frequency band 20–100 MHz, (c) MIP of the mouse ear in the frequency band: 100–180 MHz, (d) overlay of (c) in white and (a) in red to emphasize high frequencies. Scale bar: 500 μm .

Several key breakthroughs in the understanding of biological processes in the past years have been based on the advancement of imaging technology [1]. We expect that R-SOM and overall optoacoustic mesoscopy can play a key role in developmental biology and experimental genetics but also several clinical applications, including dermatology or endoscopic approaches. This will be particularly relevant in the study of adult, nontransparent organisms which cannot be accessed *in vivo* by purely optical techniques [4]. Further progress with the R-SOM technology is nevertheless required, in particular in accelerating the acquisition speed of such systems and improving the resolution and the spectral abilities of the technology.

We would like to thank Dr. Hernán Lopez-Schier for providing us with the ZF. VN acknowledges support from an ERC Advanced Investigator Award, the Kosseleck Award and the FP7 EU project FAMOS.

References

1. P. Keller, *Science* **340**, 6137 (2013).
2. P. Mahou, M. Zimmerley, K. Loulier, K. S. Matho, G. Labroille, X. Morin, W. Supatto, J. Livet, D. Débarre, and E. Beaurepaire, *Nat. Methods* **9**, 815 (2012).
3. G. J. Tserevelakis, D. Soliman, M. Omar, and V. Ntziachristos, *Opt. Lett.* **39**, 1819 (2014).
4. V. Ntziachristos, *Nat. Methods* **7**, 603 (2010).
5. M. Omar, J. Gateau, and V. Ntziachristos, *Opt. Lett.* **38**, 2472 (2013).
6. E. Strohlm, E. Berndt, and M. Kolios, *Photoacoustics* **1**, 49 (2013).
7. J. Yao and L. V. Wang, *Laser Photon. Rev.* **7**, 758 (2013).
8. K. Maslov, H. F. Zhang, S. Hu, and L. V. Wang, *Opt. Lett.* **33**, 929 (2008).
9. S. L. Chen, Z. Xie, L. J. Guo, and X. Wang, *Photoacoustics* **1**, 30 (2013).
10. J. Gateau, A. Chekkoury, and V. Ntziachristos, *J. Biomed. Opt.* **18**, 106005 (2013).
11. E. Z. Zhang, B. Povazay, J. Laufer, A. Alex, B. Hofer, B. Pedley, C. Glittenberg, B. Treeby, B. Cox, P. Beard, and W. Drexler, *Biomed. Opt. Express* **2**, 2202 (2011).
12. H. F. Zhang, K. Maslov, G. Stoica, and L. V. Wang, *Nat. Biotechnol.* **24**, 848 (2006).
13. Z. Deng, X. Yang, H. Gong, and Q. Luo, *Opt. Express* **20**, 7555 (2012).
14. M. I. Khan and G. J. Diebold, *Ultrasonics* **33**, 265 (1995).
15. X. L. Dean-Ben, D. Razansky, and V. Ntziachristos, *Phys. Med. Biol.* **56**, 6129 (2011).